



NLR-TP-2003-612

## **Low speed maximum lift and flow control**

J.W. van der Burg, J.E.J. Maseland and F.J. Brandsma

This report is based on a presentation held at the 5th ONERA-DLR Symposium ODAS 2003, Toulouse, France, 4-6 June, 2003. The report has been submitted for publication in the Elsevier Aerospace Science and Technology Journal.

This report may be cited on condition that full credit is given to NLR and the authors.

Customer: National Aerospace Laboratory NLR  
Working Plan number: A.1.A.2  
Owner: National Aerospace Laboratory NLR  
Division: Fluid Dynamics  
Distribution: Unlimited  
Classification title: Unclassified  
December 2003

Approved by author:  13/1/2004	Approved by project manager:  15/1/2004	Approved by project managing department:  16/1
--	---	--





## **Summary**

In this paper recent advances at NLR on low speed maximum lift and flow control research are reported. These three-dimensional high lift flow studies focussed on the complex flow phenomena occurring near maximum lift, the influence of geometrical complexity and Reynolds number and the effect of a Free Flying Delta Array flow control device on the high lift system performance. The potential benefits of the Free Flying Delta Array flow control device for cost effective low speed performance are quantified, based on results obtained by Computational Fluids Dynamics simulations.



## **Contents**

<b>1</b>	<b>Introduction</b>	<b>5</b>
<b>2</b>	<b>Low speed maximum lift of a three element variable sweep wing</b>	<b>6</b>
<b>3</b>	<b>Geometrically detailed modern high lift configuration</b>	<b>7</b>
<b>4</b>	<b>Free flying delta array flow control device</b>	<b>10</b>
<b>5</b>	<b>Conclusions and recommendations</b>	<b>13</b>
<b>6</b>	<b>Acknowledgements</b>	<b>14</b>
<b>7</b>	<b>References</b>	<b>14</b>
	<b>Figures</b>	<b>16</b>



## 1 Introduction

Cost effective low speed performance is playing a key role in the development of new civil aircraft where requirements on cost, safety, and environmental impact become increasingly important to maintain and improve the competitive advantage of Europe's commercial aircraft industry [9], [12]. The request for enhanced maximum lift performance measured in terms of Direct Operating Cost (DOC) is the main driver in the layout of a transport aircraft [19]. Target aerodynamic requirements such as cruise speed, range, cruise altitude, climb capability and buffet boundaries, directly influence wing design parameters, together with structural constraints like weight and manufacturability.

Increased maximum lift performance directly translates in enhanced safety. Higher performance, i.e. an increase of  $L/D$  during take-off, could be used to allow for an increased climbing rate. Higher performance of the high lift system during landing leads to a reduced landing speed and therefore increases aircraft safety. The trend in high-lift system designs is towards high-lift systems with a reduced structural and mechanical complexity compared to the more traditional high lift systems [11], [19]. Benefits of the reduced complexity are to be found in reduced cost of design, manufacture and maintenance, but also in increased safety and a reduced sensitivity to deployment location than traditional high lift systems.

The flow physics of a high lift configuration at maximum lift are complex (see also [4]). Dominant flow phenomena influencing high-lift flow are for instance: transition, flow separation, confluence of wakes, and flow unsteadiness at (post)-stall conditions as depicted in Figure 1. All these flow effects are strongly dependent on the Reynolds number, which represents the characteristic parameter between sub-scale and flight conditions, Figure 2. This figure illustrates the effect of the Reynolds number on maximum lift for a high-lift wing

For instance the type and location of the encountered flow separations in the maximum lift regime depends on the Reynolds number. For a higher Reynolds number the boundary layer is comparably thinner and this will affect these flow separations. Typical flow separations associated to wing stall are leading edge stall, trailing edge stall and/or thin airfoil stall [1].

The presence of local geometric components (needed to fly the aircraft or to conduct wind tunnel experiments) may also introduce and/or influence local flow separation. Note that at take-off condition  $L/D$  should be maximum (or drag should be minimum) which implies that flow separation should be avoided. For a landing condition  $L/D$  should also be maximum, but the necessary higher drag to minimise the deceleration distance on the ground goes associated with additional flow separations (e.g. on the flap).

Design of a cost-effective high-lift system requires parametric studies employing theoretical modelling, wind tunnels and flight tests. Data measured with sub-scale aircraft models are



extrapolated to full-scale system performance. This extrapolation process (see Figure 2) is non-linear with respect to the scaling parameter (Reynolds number). Costly design modifications late in the aircraft development program or performance shortcomings in the aircraft operation may occur due to an insufficiently accurate extrapolation. A precise understanding of the aerodynamics is therefore necessary for a successful economic and efficient design. In recent European projects extensive research has been conducted to achieve a better understanding of high lift flows [26].

In this paper two CFD studies are presented which focus on the occurrence of critical flow phenomena at low-speed maximum lift at wind tunnel conditions and a third CFD study is presented that researches a flow control device that could lead to a potential improvement in maximum lift performance. The CFD studies are arranged such that they consider an increase in flow complexity.

## 2 Low speed maximum lift of a three element variable sweep wing

The first CFD study<sup>1</sup> has been focussed on the improvement of knowledge concerning specific CFD technologies, such as suitable turbulence models, grid strategies, for studying three-dimensional high-lift flows. The 'Aile à Flèche Variable' (AFV) configuration as designed by ONERA has been selected as the test geometry. The configuration is composed of a 3-element variable sweep wing with an untapered, constant section, untwisted planform. A sweep angle  $\Lambda = 40^\circ$  is selected for which the brackets and wing tip are aligned with the undisturbed flow. The slat and flap deflection angles for landing are defined as  $\delta_s = 30^\circ$  and  $\delta_f = 20^\circ$ , respectively. The AFV configuration has been tested in the ONERA F1 wind tunnel. The arrangement of the model in the wind tunnel is depicted in Figure 3. The geometrical definition of the computational model represents a simplified geometry in which the slat brackets and the flap track fairings have not been modelled. Furthermore, the static deformation of the model due to the aerodynamic forces is not accounted for.

Fully turbulent flow is assumed in the calculations, as measurements of laminar/turbulent transition were not available. Flow conditions are:  $M_\infty = 0.146$  and  $Re = 3.31 \times 10^6$ . Transition calculations performed by ONERA indicate that leading-edge contamination occurs for the main-wing at all selected incidence angles. The boundary layers are therefore considered to be fully turbulent (in the flow computations). NLR has conducted the turbulent flow simulations on an unstructured hybrid grid. Grid resolution in the vicinity of the slat is shown in Figure 4. A comparison of the experimental and predicted aerodynamic forces is presented in Figure 5 as

---

<sup>1</sup> The work reported here has been carried out in the frame of the GARTEUR Action Group 36 on three-dimensional high-lift computations in collaboration with the partners ONERA, FOI, QINETIQ and EADS-Germany (see also [23], [26]).



a function of the angle of attack. The experimental results originate from balance measurements corrected for wind tunnel wall influences and the calculated results are obtained by integrating both the pressure and viscous forces. The computed angle of attack for maximum lift matches the experimental angle of attack for maximum lift. It can be observed that the computed maximum lift value differs approximately 4.6% from the experimental value. The skin friction distribution and the integrated skin-friction lines are depicted in Figure 6 for  $\alpha = 37.81^\circ$ . The stall mechanism as illustrated by the skin-friction lines for the maximum lift case is flow separation on the main-wing element starting at the tip. A separation line and a reattachment line are noticeable on the main wing. Interaction of the separated flow of the main-wing with the flow over the flap is not observed.

### 3 Geometrically detailed modern high lift configuration

Geometrical detail of the high-lift system can strongly influence maximum lift performance. Some examples are shown in [4]. In view of this NLR has conducted a CFD study<sup>ii</sup> that has focussed on the influence of flap track fairings on lift near stall at low Reynolds number wind tunnel conditions, and at the influence of the Reynolds number effect. Of course, in a wind tunnel experiment it is rather difficult to discriminate the effect of the flap track fairings. The focus of the study has been particular directed towards the identification of critical flow processes affecting high lift flows.

To assess the influence of the flap track fairings a CFD geometry of the KH3Y model has been created which includes the fuselage, main wing, a full span slat, a part span flap and five flap track fairings (Figure 7 shows the KH3Y model in the LSWT wind tunnel) and a configuration without flap track fairings (not shown)<sup>iii</sup>. The cove region at the location of the flap track fairings is left open. The slat, main wing and flap have finite trailing edge thickness with an approximate size of  $3 \times 10^{-3}$  t/c. The tips of the slat, wing and flap are modelled as a flat plate (no rounding of tips and/or trailing edges has been adopted). A hybrid computational grid having approximately 8 million nodes has been created using the FASTFLO CFD system [2]. Flow computations have been conducted at a Mach number of  $M_\infty = 0.174$  and Reynolds number  $Re_L = 1.34 \times 10^6$  based on a reference chord length  $L = 0.34$  m. Wind tunnel walls and the peniche

<sup>ii</sup> This CFD study has been carried out in the framework of the EU Eurolift project. A consortium of European industries and research institutes led by Airbus-Germany has initiated the Eurolift project [5], [24], [25]. The main objective of this project is to reduce the time and cost of the design process of high lift systems by development of more reliable computational and design tools. To this purpose an extensive numerical and experimental campaign, including low Reynolds number tests in the low speed wind tunnel (LSWT) in Bremen and high Reynolds number measurements in the cryogenic wind tunnel European Transonic Windtunnel ETW, has been carried out. An overview with the outcome of the Eurolift project results can be found in the references [6], [18] and [21].

<sup>iii</sup> In the CFD computations without flap track fairings a computational hybrid grid created by FOI has been used.



have not been modelled. In order to examine the main critical processes affecting high lift flow it was decided at this stage not to specify transition location(s) in the flow computation. In the LSWT wind tunnel experiments a smooth stall behaviour has been found, see Figure 8, which seems to largely influenced by main wing trailing edge flow separation, see Figure 12. Specification of laminar/turbulent transition specification could be important here and for instance implicate a reduced boundary layer thickness and postponed flow separation. In the flow computations a sufficient number of multigrid steps (in the order of 6000 steps ) have been taken to converge the aerodynamic coefficients (for the steady-state cases, i.e. the non post-stall flow conditions).

The CFD study has been conducted at a low Reynolds number (namely for LSWT wind tunnel conditions) at take-off conditions. Computed lift curves are shown in Figure 8. In the linear range the difference in lift compared to the experimental values is  $\Delta C_L \approx 0.07$ . For the configuration with flap track fairings maximum lift is occurring for angle of attack larger than  $18.5^\circ$ . The maximum lift point is close to  $18.5^\circ$  degrees since the slope of the lift curve is already levelling off. For the configuration without flap track fairings an abrupt stall behaviour is observed; the maximum lift point is found at  $\alpha=18.5^\circ$ .

For the configuration with flap track fairings the stall behaviour is initially mainly triggered by a flow separation on the outboard part of the main wing near the trailing edge, see Figure 10. For  $\alpha=18.5^\circ$  a mid-chord separation line and a reattachment line are present. For lower angles of attack the separation line and reattachment line are located closer to the main wing trailing edge. The flow separation is a cross flow separation. Oil flow measurements confirm the presence of flow separation at the outboard main wing. The flow separation is also indicated in the wind tunnel measurement by the tufts mounted on the wind tunnel model. Despite the unacceptable implications for aircraft controllability (see also [19]) due to a flow separation on the outboard high lift wing, the main wing trailing edge stall behaviour appears to explain the gradual reduction in the lift curve slope. In the outboard wing cross section, designated as section DV10 (see also Figure 11), it can be observed that the turbulent kinetic energy reaches a maximum value at a point above the main wing trailing edge. In Figure 9 the distribution of the turbulent kinetic energy normal to the surface at  $x=1.88\text{m}$  on outboard section DV10 (upstream of the separation line) is depicted. It shows that the wall-normal kinetic boundary layer profile has been well resolved at this location.

In the CFD study the maximum lift point is found for an angle of attack of  $\alpha=18.5^\circ$ . At post-stall conditions  $\alpha=20^\circ$  the flow has become unsteady around a fixed lift point. It appears that the flow on the slat and the upper main wing near the kink section has separated (not shown).

In order to study the effect of grid resolution a CFD computation has been conducted on a twice-refined unstructured hybrid grid having approximately 16 million grid nodes for angle of attack  $\alpha=16^\circ$ . Compared to the initial hybrid grid the lift has moderately increased on the refined



hybrid grid, see also Figure 8. In the computed flow solution it appears that a massive flow separation occurs on the upper wing near the fourth flap track (see Figure 12). This corresponds to the experimental oilflow results shown. In particular the underwing mounted flap track fairings seem to have an upper wing effect by influencing the slat-wing gap flow. Furthermore, regions of low skin friction can be observed near the trailing edges of the flap track fairings. The flow computation illustrates the clear need for sufficient grid resolution in order to capture the relevant flow separation(s).

For the configuration without the flap track fairings, see also Figure 10, the computed flow effect causing lift break down is leading edge flow separation on the mid-span slat (not shown). This slat separation induces a lift break down on the main wing. The flow separation on the outboard part of the main wing is also present (no reattachment line is observed), but seems to be less dominant. This lift break down behaviour supports the more abrupt change of the lift curve at maximum lift.

These observations lead to the conclusion that the presence of the flap track fairings has a significant influence on the maximum lift behaviour for the LSWT Reynolds number condition. Different complex flow phenomena near stall have been observed. More CFD studies will be needed to single out the effects of geometrical detail (like the presence of slat tracks, wind tunnel walls and peniche<sup>IV</sup>), grid resolution, transition and flow unsteadiness.

Since maximum lift behaviour is strongly related to the Reynolds number wind tunnel experiments have been conducted with the KH3Y model in the ETW. To study the effect of a higher Reynolds number flow computations have been conducted for a geometrically simplified CFD geometry (of the KH3Y model) which has a full span flap, but where the flap track fairings are not modelled. The flow conditions are: Mach number  $M=0.176$  and Reynolds number  $Re_l=15.022 \times 10^6$  based on a reference chord length  $L=0.34$  m.

Abrupt stall behaviour is observed in both the computed and experimental lift curves, see Figure 13. The difference in lift in the linear range is approximately 5%. In the flow computations maximum lift is found for  $\alpha=22^\circ$ , and occurs at a higher angle of attack compared to the ETW experiment. In the flow computations it is observed that the lift breaks down on the outboard part of the main wing at  $\alpha=23^\circ$ . Beyond maximum lift, the flow becomes unsteady.

Computed and measured pressure coefficient distributions at sections DV6 (mid-span) and DV10 (outboard location) are shown in Figure 14. In the linear range of the lift curve, i.e. until angle of attack  $\alpha=18.5^\circ$  (see also Figure 14), generally a good agreement with the experimental data is observed. However, for larger angles of attack ( $\alpha=20^\circ$  is shown) a significant difference with the ETW experimental results occurs. In the wind tunnel experiment for  $\alpha=20^\circ$  the flow on

---

<sup>IV</sup> A peniche has been mounted between the KH3Y high-lift half model and the wind tunnel wall. The peniche is needed to reduce the influence of the wind tunnel wall boundary layer on the flow around the half model.



the outboard section DV10 has separated due to slat separation. In the flow computation DV6 and DV10 are not separated. For  $\alpha=21^\circ$  (not shown) section DV6 has separated as well (in the experiment), but the lift on section DV10 has been re-established again. This phenomenon has not been found in the flow computations.

The measured Reynolds effect is reproduced in the computations in a sense that a higher stall angle of attack is found. This could be explained by arguing that for a higher Reynolds number the boundary layer is thinner, and hence flow separation (on the main wing) is postponed. In the flow computation it is observed that flow separation on the slat triggers lift break down on the main wing. This flow separation occurs at a higher angle of attack compared to experiment.

Different effects may play a role: firstly, wing deformation for the highest angles of attack, as a result of the high dynamic pressure needed to achieve the wind tunnel Reynolds number. This leads to different gaps and overlaps and a different maximum lift behaviour. Secondly, the presence of specific geometric components such as wind tunnel walls, peniche, and/or slat tracks may influence maximum lift behaviour. A non-uniform flow field caused by the presence of wind tunnel walls and/or boundary layer suction could also have an influence on the stall behaviour. Thirdly, in a high-lift wind tunnel experiment laminar flow can persist to high Reynolds numbers and this can have a significant influence. Hence, the effect of laminar/turbulent transition should be taken into account (in a flow computation).

The computed stall behaviour in the high Reynolds number study (slat separation) is different in terms of location of the encountered flow separation in comparison to the low Reynolds number study (outboard part of main wing). More research will be needed here as well to study and explain the differences between the computed and measured stall behaviour. Important will be to be able to understand the effect of high-lift wing deformation which will play a role not only in ETW wind tunnel experiments, but also in flight conditions.

#### **4 Free flying delta array flow control device**

A key problem in pursuing either an increased low speed high-lift performance or a less complex high-lift system is to avoid flow separation in the flows about the high-lift system. The application of flow control devices to high-lift systems designed to avoid flow separation became a subject of many investigations during the last decade. Most of these studies like the work on micro vortex generators presented in [14] and [15], and the work on airjet vortex generators [10] focus on mitigating boundary layer separation on the flap at take-off or landing settings. However, maximum lift for high-lift systems is a complex phenomenon that, especially at flight Reynolds numbers, is not always governed the flap boundary layer separation but by other effects like the breakdown of the wake of the main wing above the flap. To illustrate wake breakdown the computed flow field for a high-lift three-element airfoil at a high angle of attack

$\alpha=32^\circ$  is shown in Figure 16. A flow control device that extracts part of its beneficial effects from influencing the main wing wake flow is the lift-enhancing tab placed in the cove area at the main wing trailing edge as demonstrated in [3], [20] and [22].

A CFD study<sup>V</sup> has been conducted for a novel flow control device, called the free flying delta array (FFDA) that is aimed at controlling both the flap boundary layer development and the wake flow of the main wing. The FFDA device consists of an array of delta wings placed in the gap between the main wing and the flap at take-off and landing settings (see Figure 17). Each sharp edged delta wing generates a pair of counter rotating vortices. As is demonstrated in [14] counter rotating vortices are slightly more effective in controlling the flap boundary than co-rotating vortices. The anticipated effect of the vortex pairs on the main wing wake flow is that the flow will be turned towards the flap surface, which is basically the same effect as the lift-enhancing tabs of [3], [20] and [22], but now realised with vortices of which the axes are aligned with the main flow rather than perpendicular to the flow direction. The complexity of the associated flow phenomena for the FFDA device requires CFD simulations based on the Navier-Stokes equations right from the start of the design process.

The size of the delta wings is chosen to be 2% of the wing reference chord of the baseline section (with slat and flap retracted) which is a typical size for a vortex generator. Most effective in generating vortices are delta wings with a sharp leading edge. In order to keep the design of the high-lift system as simple as possible the delta wings are assumed to be in a fixed position with respect to the flap (deployment mechanisms are too complex and have the additional risks of failure). The consequence is that the delta wings should be stowed in the cove when the flap is retracted and the design freedom of the position of the delta wing is narrowed to a region close to the leading edge of the flap. The curved flow in the cove region leads to large variation of the local angle of incidence along the leading edge of such planar delta wing and vortex breakdown close to the trailing edge of the delta wings was observed, destroying the beneficial effects of the FFDA device.

The geometry of a non-planar delta-wing shape that has been the subject of a more detailed investigation is presented in Figure 17. It is a  $65^\circ$  cropped delta wing with a curved centre-plane that basically follows the flap upper surface. This delta wing is placed at some distance from the flap and rotated over  $10^\circ$  with respect to the flap surface tangent. The rotation angle is selected such that the vortices are strong enough to have the desired effects on the flap boundary layer at the main wing wake flow, but should be limited to avoid vortex breakdown.

The effect of the FFDA concept is evaluated by performing simulations for a three-dimensional configuration consisting of a constant chord unswept wing of limited span and with the HELIX

---

<sup>V</sup> The work presented here has been carried out partly within the framework of the EU project HELIX (see [8]) where innovative aerodynamic high-lift concepts have been developed.



2D baseline three-element airfoils as the section. One delta wing is placed above the flap leading edge in the cove area. Two planes at constant span position form the boundary of the computational domain. On these planes periodic boundary conditions have been imposed. In that way the effect of an infinite array of delta wings on an unswept constant chord wing of infinite span in landing and take-off configuration is simulated. A CFD study has been carried out with the multi-block CFD system ENFLOW [13].

The effects of the FFDA on the flap boundary layer and the main wing wake are demonstrated in Figure 18 for the landing configuration showing Mach number distributions and streamline patterns in the centre-plane for the clean configuration and the configuration with the FFDA. The flow conditions are: Mach-number  $M_\infty = 0.18$ , angle of attack  $\alpha = 18^\circ$  and Reynolds number  $Re = 19.0 \times 10^6$ . The (projected) streamlines suggest a trailing edge separation for the clean configuration starting at approximately 75% flap chord. When the FFDA is applied this flow separation is reduced largely in size to just a small pocket of re-circulating flow just downstream of the (blunt) flap trailing edge. The main wing wake is thickened in the centre plane due to a downward directed velocity induced by the vortices. It should be kept in mind that Figure 18 only gives a two-dimensional view on the separation. For the configuration with FFDA the flow is essentially three-dimensional. The 2D separation for the clean configuration, with the separation line perpendicular to the flow direction, is replaced by an array of three dimensional flow separations with the separation lines aligned with the main flow direction. This feature is demonstrated in Figure 19. The flow pattern on the flap for the landing configuration is visualised by means of integrated skin friction lines. Underneath each vortex a small flow separation is induced as can be seen from the separation lines on the flap surface. Re-attachment is observed in the centre-plane between each pair of counter rotating vortex and in the periodic plane between two neighbouring pairs of vortices.

The aerodynamic effectiveness of the FFDA device is demonstrated in Figure 20. Here computed lift- and drag polars for the landing configuration are presented with and without FFDA. Although, maximum lift has not yet been computed for the configuration with FFDA, it is anticipated that application of the FFDA could lead to an increased  $C_{Lmax}$ . The FFDA not only generates an increased lift at constant angle of attack, but also a slight drag reduction at constant lift is found. The L/D values for the landing configuration have been increased by approximately 20% to 30% over the linear range that has been computed.

The results obtained in the present study have been translated to effects on the HELIX Baseline Aircraft by means of an engineering method. The potential gain in aerodynamic performance is shown in Figure 21 where the estimated drag polars for both take-off and landing configuration of the baseline aircraft with FFDA are compared to those of the clean baseline aircraft. The estimated effect of the FFDA is an increase in maximum lift of approximately  $\Delta C_{Lmax} = 0.0338$  at the safety take-off speed defined by  $C_L = C_{Lmax}/1.13^2$ , a drag reduction is obtained of  $\Delta C_D = -0.0043$ . Also for the landing configuration a gain in maximum lift predicted but now



$\Delta C_{L_{\max}}=0.0348$ . For the safety approach speed characterised by  $C_L = C_{L_{\max}}/1.23^2$  a drag reduction of  $\Delta C_D = -0.0089$  by applying the FFDA is predicted.

Analysing these results in terms of a simplified DOC model show a 5% improvement of the second climb segment gradient compared to the baseline aircraft with no increase of the take-off speed, where also the landing speed shows a slight improvement. It should be mentioned here that in the present study the FFDA device has been applied to an already optimised conventional high-lift system that for its design conditions does not exhibit massive flow separations nor wake breakdown above the flap. It is to be expected that novel high-lift systems designs aimed at either a reduction of geometric complexity or at an increased aerodynamic performance at the same cost will gain even more from the FFDA flow control device.

## 5 Conclusions and recommendations

Detailed CFD studies of three-dimensional high-lift flows, as presented in this paper, have provided insights into the complex flow phenomena occurring near low speed maximum lift conditions. For two swept high-lift wings (a three element variable sweep wing and a geometrically detailed modern high lift configuration) flow separation on the outboard part of the main wing element has been computed at low Reynolds number wind tunnel conditions. It has been illustrated that the presence of the flap track fairings has a significant influence on the stall behaviour near maximum lift.

When proceeding to a higher Reynolds number the dominant stall mechanism is different. In both the wind tunnel experiment and flow computation only flow separation on the slat is found. Due to the high loading of the high-lift wing in the ETW wind tunnel the aero-elastic deformation near maximum lift may play an important role. It is concluded that further research on stall behaviour will be needed to discriminate between the influence of high-lift configuration or wind tunnel related geometrical components and computational modelling effects (transition, turbulence model or grid resolution). It is recommended that fluid-structure interaction for a high-lift wing should be modelled in order to understand the effects of high-lift wing deformation, where local changes in flap (setting) geometry should be accounted for. A novel high-lift system design including a promising Free Flying Delta Array flow control device to obtain the required aerodynamic performance has been studied. It is illustrated that the Free Flying Delta Array could have a potential for cost-effective high-lift performance in terms of Direct Operating Costs.

The conducted CFD studies form part of a larger research framework at NLR aimed at enhancing flight safety under high-lift conditions. Future work will focus on the modelling of surface roughness effects to study the effect safety implications of for instance icing conditions



[7]. Further improvements in high lift performance can be achieved by continued high-lift CFD research focussed on enhancing flow physics modelling to understand the dominant stall mechanism and the Reynolds number effect (see also [16]).

## 6 Acknowledgements

The authors wish to thank Koen de Cock for providing useful comments, suggestions and feedback concerning the subject of investigation in this report.

## 7 References

- [1] Berg, B. van den, Reynolds number and Mach number effects on the maximum lift and the stalling characteristics of wings at low speeds, NLR TR 69025 U, March 1969.
- [2] Burg, J.W. van der, Weide, E.T.A. van der, Short turnaround time turbulent flow computations for complete aircraft configurations, NLR Technical Publication 2002-270, ICAS 2002 Congress, Toronto, September 2002. Also issued as NLR Technical Publication 2002-270.
- [3] Carrannanto P.G., Storms, B. L., Ross, J.C., Cummings, R.M., Navier-Stokes analysis of lift-enhancing tabs on multi-element airfoils, Aircraft Design, Vol. 1, No. 3, pp. 145-158, 1998.
- [4] Dam, P. van, Vijgen, P., Aerodynamic design improvements: high-lift systems and cruise performance, course Notebook I and II, University of Kansas Continuing Education (KUCE), 2001.
- [5] European high lift programme Eurolift, Annex I "Description of work" of the EC Growth Project GRD1-1999-10015, December 2001.
- [6] Eliasson, P. (2003), CFD improvements for high lift flows in the European Project Eurolift, AIAA 2003-3795, Orlando, 2003.
- [7] Feo, A., Henry, R., Ice accretion and performance degradation on airfoils in high lift configurations, paper presented at the KATnet/GARTEUR High Lift Workshop, Stockholm, Sweden, September, 2002.
- [8] Galpin, S.A., Melin, T., HELIX: Innovative high-lift aerodynamic concepts, an overview, paper presented at the KATnet/GARTEUR High Lift Workshop, Stockholm, Sweden, 17-19 September, 2002.
- [9] Henke, R., High lift drivers and process, paper presented at the KATnet/GARTEUR High Lift Workshop, Stockholm, Sweden, September 2002.
- [10] Innes, F., Percy, H. H., Sykes, D. M., Improvement in the performance of a three

- element high lift system by the application of airjet vortex generators, *Aeronautical Journal*, August/September 1995, pp. 265- 274, 1995.
- [11] Jupp, J., Keep it simple and get it right, paper presented at the KATnet/GARTEUR High Lift Workshop, Stockholm, Sweden, 17-19 September, 2002.
- [12] Kafyeke, F., Pepin, F., Kho C., Development of high lift systems for the Bombardier CRJ 700, in proceedings of the ICAS 2002 Congress, Toronto, September 2002.
- [13] Kok, J.C., Spekreijse, S.P., Efficient and accurate implementation of the  $k-\omega$  turbulence model in the NLR multi-block Navier-Stokes system, presented at the ECCOMAS 2000 Conference, Barcelona, Spain, 11-14 September 2000, Also issued as NLR Technical Publication 2000-144.
- [14] Lin, J. C., Robinson, S. K., McGhee, R. J., Separation control on high-lift airfoils via micro-vortex generators, *Journal of Aircraft*, Vol. 31, No. 6, pp. 1317-1323, 1994.
- [15] Lin, J. C., Control of turbulent boundary-layer separation using micro-vortex generators, 30<sup>th</sup> AIAA Fluid Dynamics Conference, Paper AIAA 99-33593, 1999.
- [16] Moens, F., Rudnik R., Quest J., Burg, J.W. van der, Perraud J., Hansen H., Eliasson P., High-lift R&TD Guidelines, An Eurolift View, Technical report produced in the Eurolift project, June 2003.
- [17] Oskam, B., Laan, D.J., Volkers, D.F., Recent advances in computational methods to solve the high-lift multi-component airfoil problem, NLR MP 84042 U, 1984.
- [18] Perraud, J., Moens, F. and Seraudie, A., Transition on a high lift swept wing in the European Project Eurolift, AIAA 2003-3796, Orlando, Florida, 2003.
- [19] Reckzeh D., Aerodynamic design of the high-lift wing for a Megaliner aircraft, *Aerospace Science and technology* 7, pp. 107-119, 2003.
- [20] Ross, James C., Storms, Bruce L., Carrannanto, Paul G., Lift-enhancing tabs on multi-element Airfoils, *Journal of Aircraft*, Vol. 32, No.3, pp. 649-655, 1995.
- [21] Rudnik, R. (2003) CFD assessment for 3D high lift flows in the European project Eurolift, AIAA 2003-3794, Orlando, Florida, 2003.
- [22] Storms, Bruce L., Ross, James C., Experimental study of lift-enhancing tabs on a two-element airfoil, *Journal of Aircraft*, Vol. 32, No. 5, pp. 1072-1078, 1995.
- [23] Thibert, J.J., The Garteur role for high lift research in Europe, paper presented at the KATnet/GARTEUR High Lift Workshop, Stockholm, Sweden, 17-19 September, 2002.
- [24] Thiede, P., Recent achievements of the European high lift Programme Eurolift, on CD-rom of the CEAS Aerospace Aerodynamics Research conference, Cambridge, June 2002.
- [25] Thiede, P., Overview on the European high lift Programme Eurolift, paper presented at the KATnet/GARTEUR High Lift Workshop, Stockholm, Sweden, September, 2002.
- [26] Williams, B., Garteur Aerodynamics: Fundamental research complementing EC programmes, on CD-rom of the CEAS Aerospace Aerodynamics Research conference, Cambridge, June 2002.

Figures

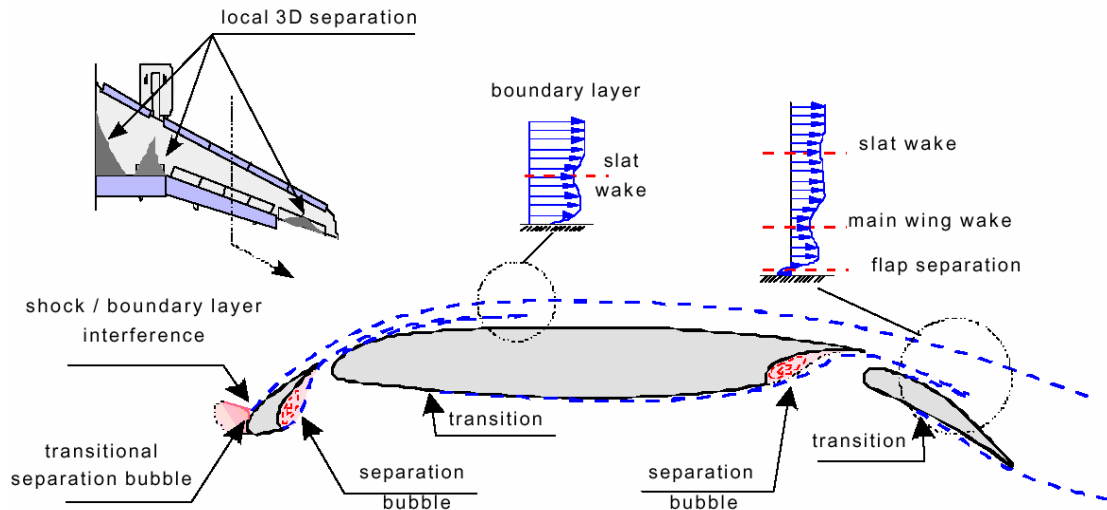


Figure 1 Complexity of the flow physics of a high lift system (from Ref. [5] or [19]). The figure illustrates the different flow phenomena that may occur for a high-lift wing, such as for instance transition, flow separation, separation bubbles and wake confluence.

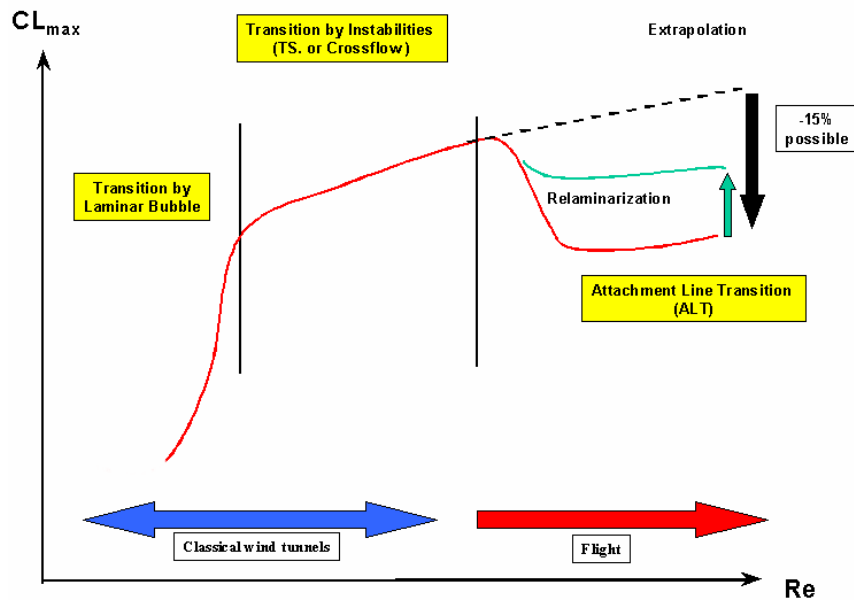


Figure 2 Maximum lift (red line) as a function of the Reynolds number (from Ref. [5]) for a high lift swept wing. On a swept wing many transition mechanisms (depending on the Reynolds number) can occur that can lead to breakdown of laminar to turbulent flow. A subdivision has been made in a lower Reynolds number range (classical wind tunnels) and a higher Reynolds number range (flight conditions). Contamination at the leading edge stems from turbulence produced at a fuselage/wing juncture, which travels over the high-lift wing contaminating otherwise laminar flow. If the Reynolds number of the attachment line boundary layer is greater than some critical value, this contamination leads to turbulent flow over the complete wing reducing maximum lift. A significant drop in maximum lift (15% possible) at flight Reynolds numbers can be experienced. Relaminarization of the boundary layer can enhance the maximum lift level again.

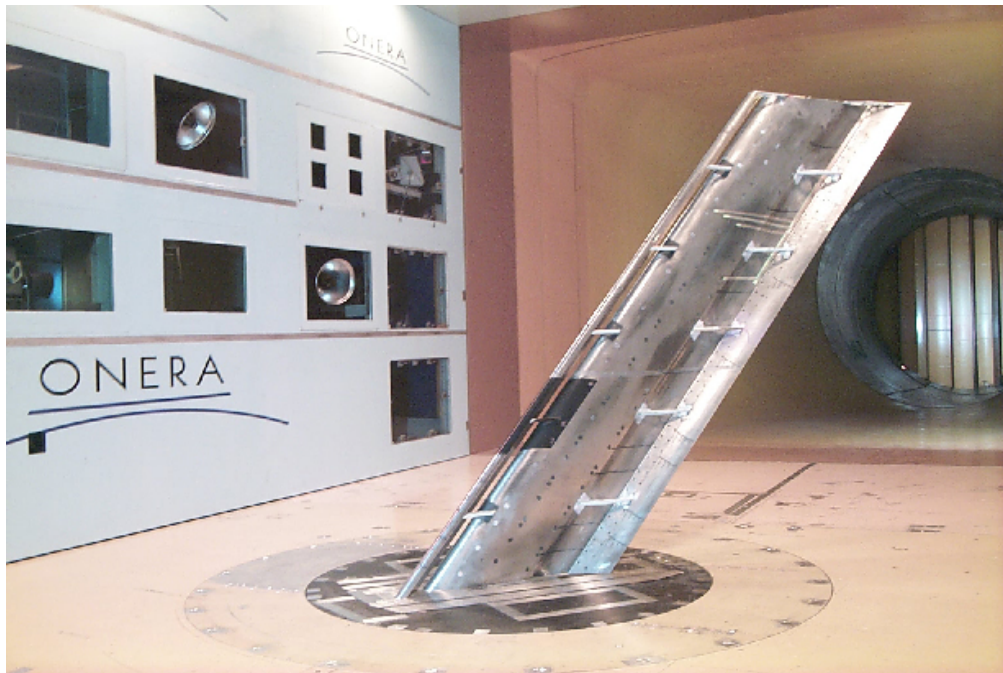


Figure 3 The Aile à Flèche Variable (AFV) high-lift wind tunnel model mounted in the ONERA F1 wind tunnel (courtesy of ONERA)

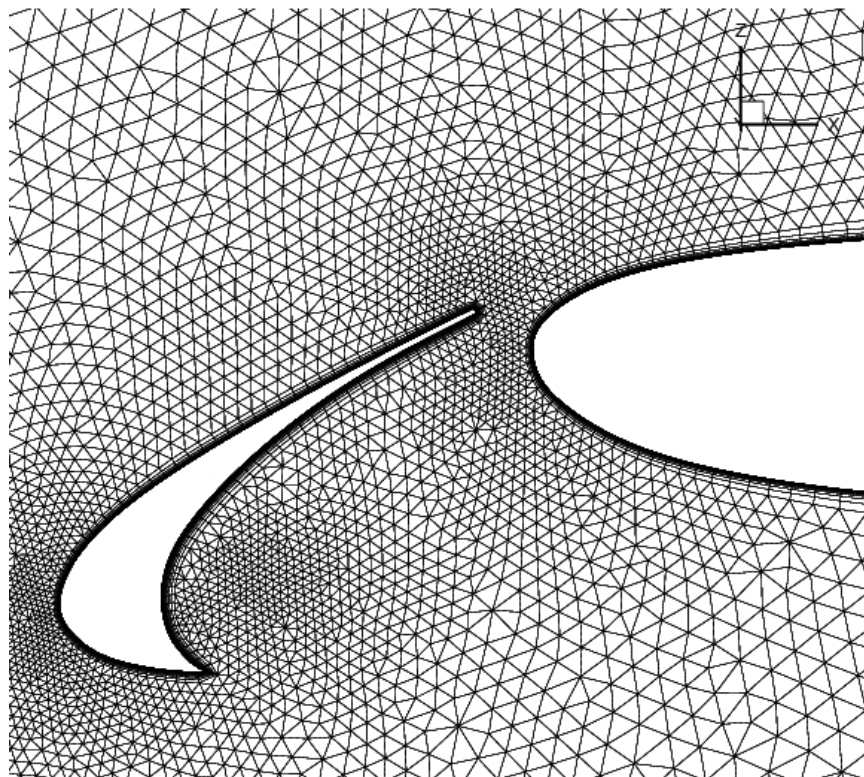


Figure 4 Grid point distribution in the vicinity of the slat on the symmetry plane for the Aile à Flèche Variable (AFV) high-lift wind tunnel model.

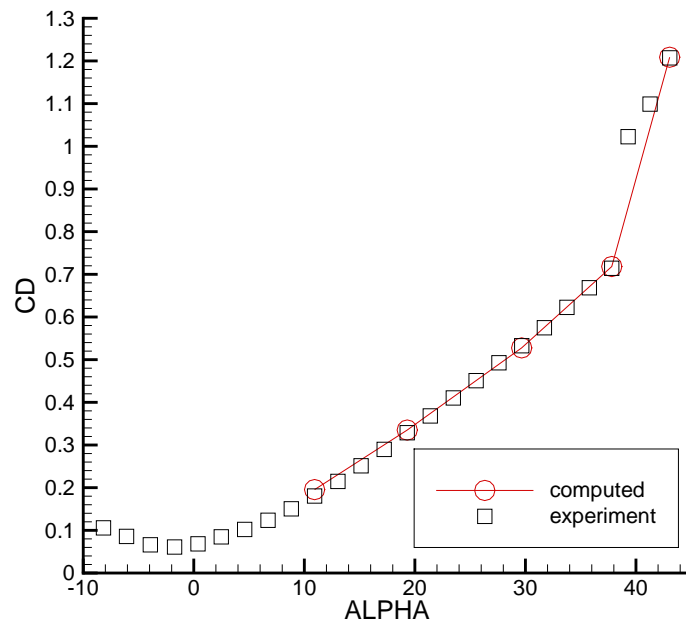
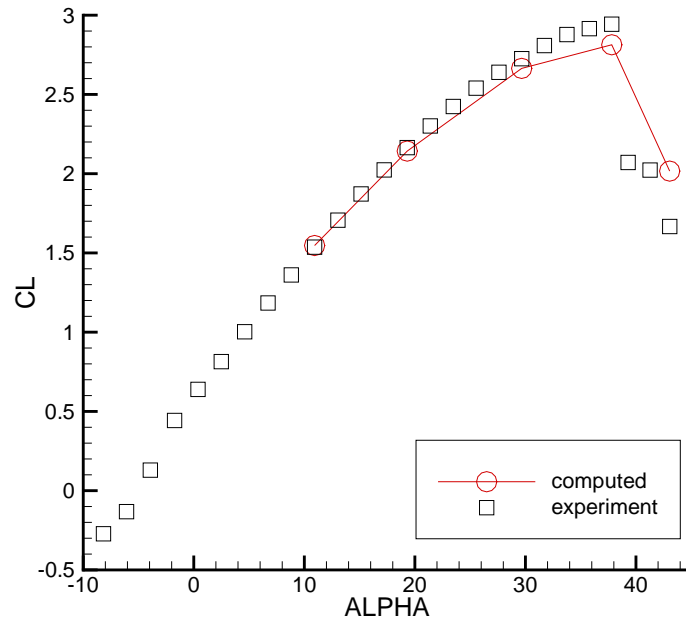


Figure 5 Comparison of the lift polar and drag polar for  $M_\infty = 0.146$  and  $Re = 3.31 \times 10^6$  for the Aile à Flèche Variable (AFV) high-lift wind tunnel model (Experimental data points are shown for the range  $-10^\circ < \alpha < 45^\circ$  in steps of  $\Delta\alpha = 2^\circ$ ).

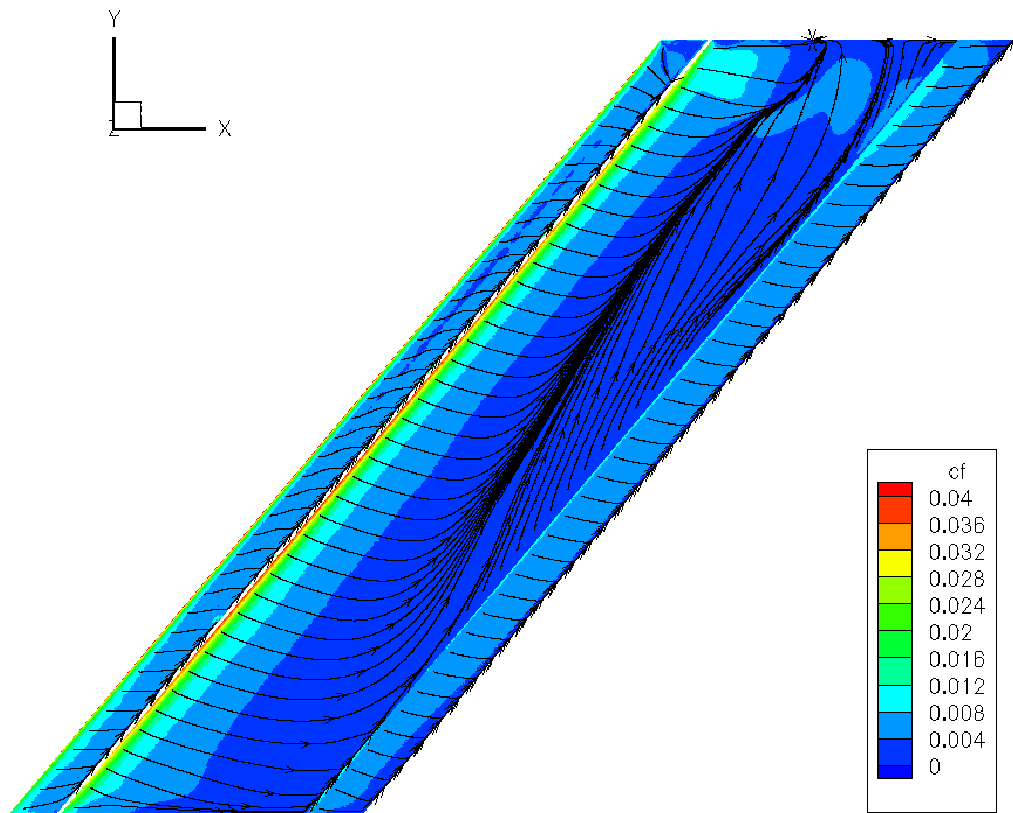


Figure 6 Computed skin-friction coefficient and integrated skin-friction lines for  $\alpha=37.81^\circ$  for the Aile à Flèche Variable (AFV) high-lift wind tunnel model.

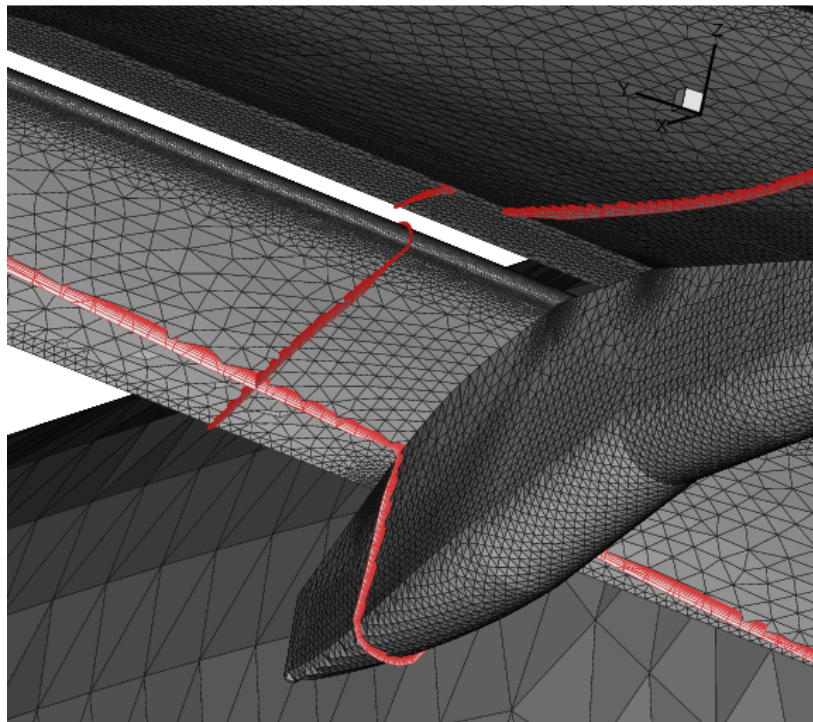
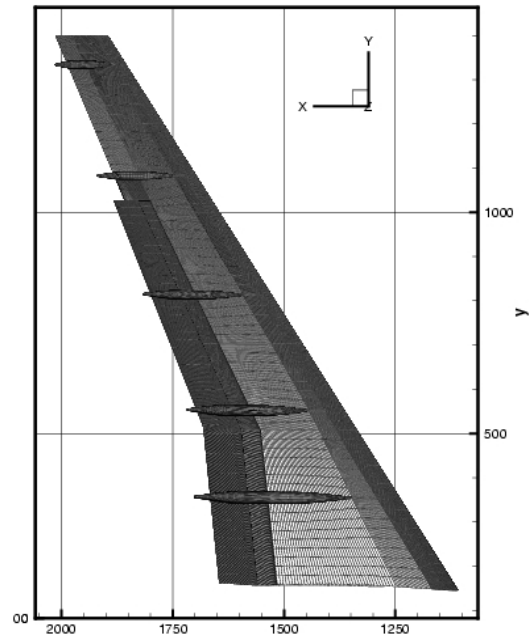


Figure 7 i) KH3Y wind tunnel model mounted in the LSWT wind tunnel in Bremen (top left). The wind tunnel model is a half model mounted on a peniche; ii) CFD geometry of the KH3Y wind tunnel model defined in terms of structured surface patches (top right); iii) Close-up view of the computational (triangular) surface grid near the second flap track fairing mounted under the high-lift wing (bottom). Cross-sections at  $x=\text{constant}$  and  $y=\text{constant}$  with the prismatic boundary layer grid are shown (in red). The cross sections illustrate the height of the generated prismatic grid (needed to resolve the boundary layer).

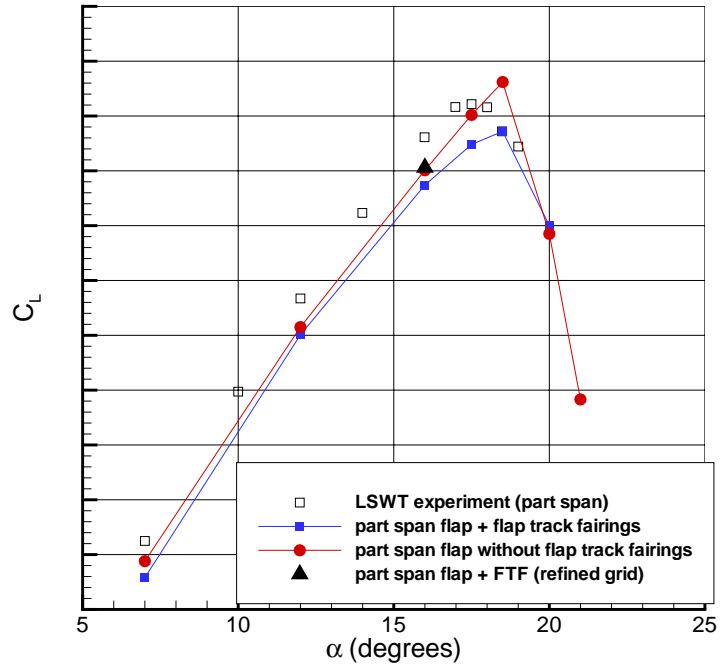


Figure 8 Computed lift curves for two geometrical variants of the KH3Y model, i.e. a part span flap configuration with and without flap track fairings, compared to the measured lift curve in the LSWT (for configuration with flap track fairings)

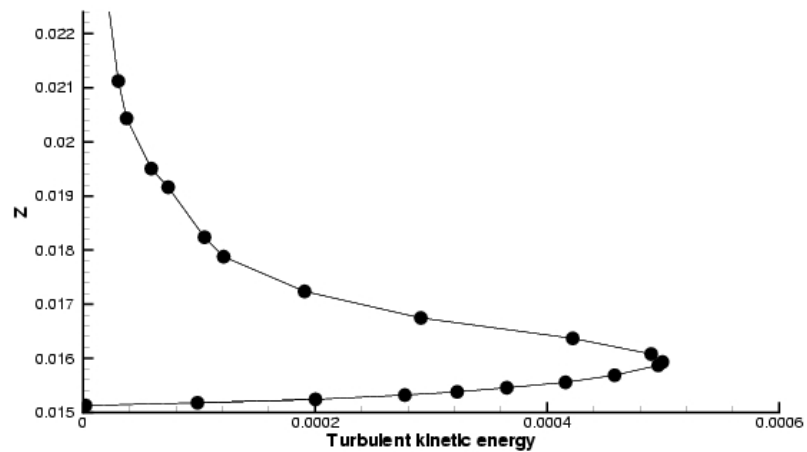


Figure 9 Computed wall-normal (z-direction) turbulent kinetic energy distribution on  $x=1.88\text{m}$  at section DV10. Sufficient grid resolution has been employed to resolve the turbulent kinetic energy profile.

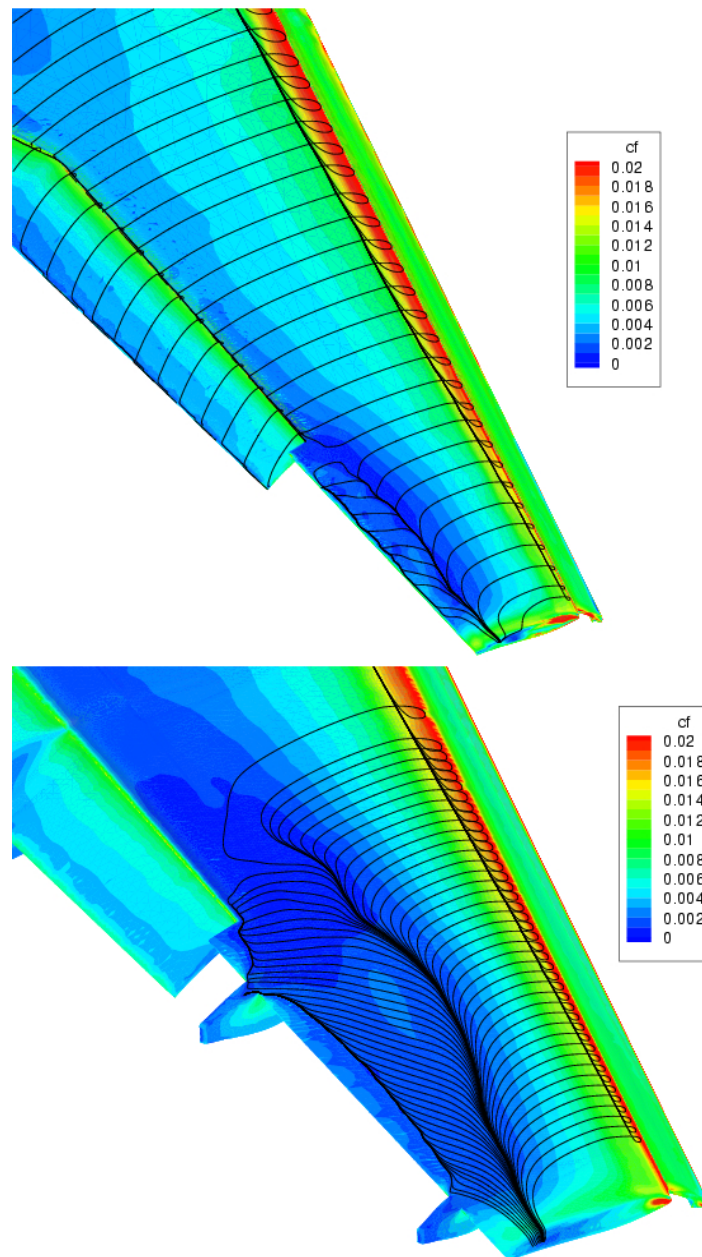
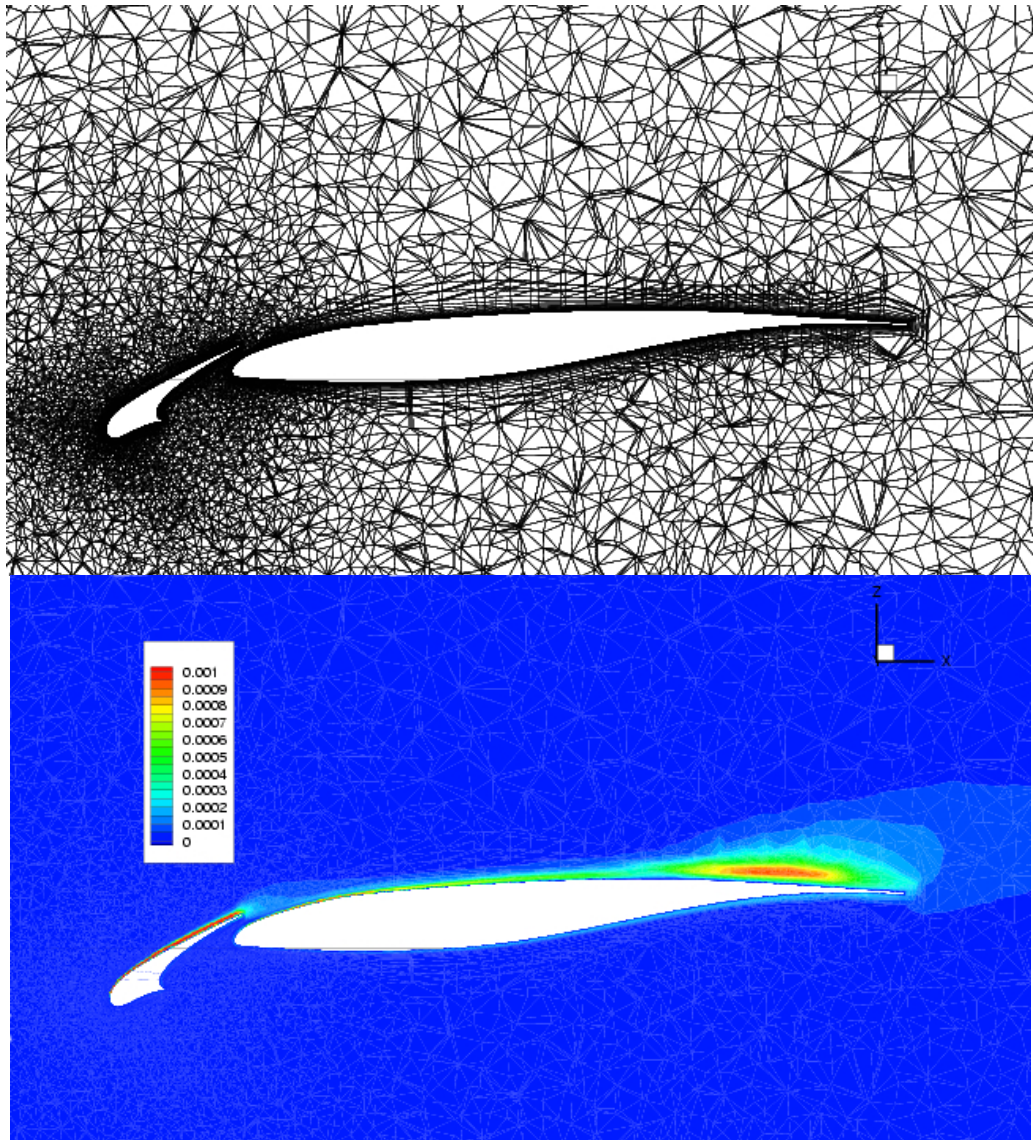


Figure 10 Close-up of the skin friction distribution and skin friction lines for two geometrical variants of the KH3Y model: a part span flap without (top) and with (bottom) flap track fairings installed for  $M=0.174$ ,  $\alpha=18.5^\circ$ ,  $Re=1.34 \times 10^6$ . Low skin friction values are observed on the outboard portion of the main wing with flap track fairings installed. A separation line and a reattachment line are present.



*Figure 11 Cross section at section DV10 (outboard wing section) of the computational grid and the turbulent kinetic energy distribution; a flow-separated region on the main wing can be observed near the main wing trailing edge; Cross section DV 10 is located between the 4<sup>th</sup> and 5<sup>th</sup> flap track fairing (located at the outer wing) at spanwise location  $y \approx 1250\text{mm}$*

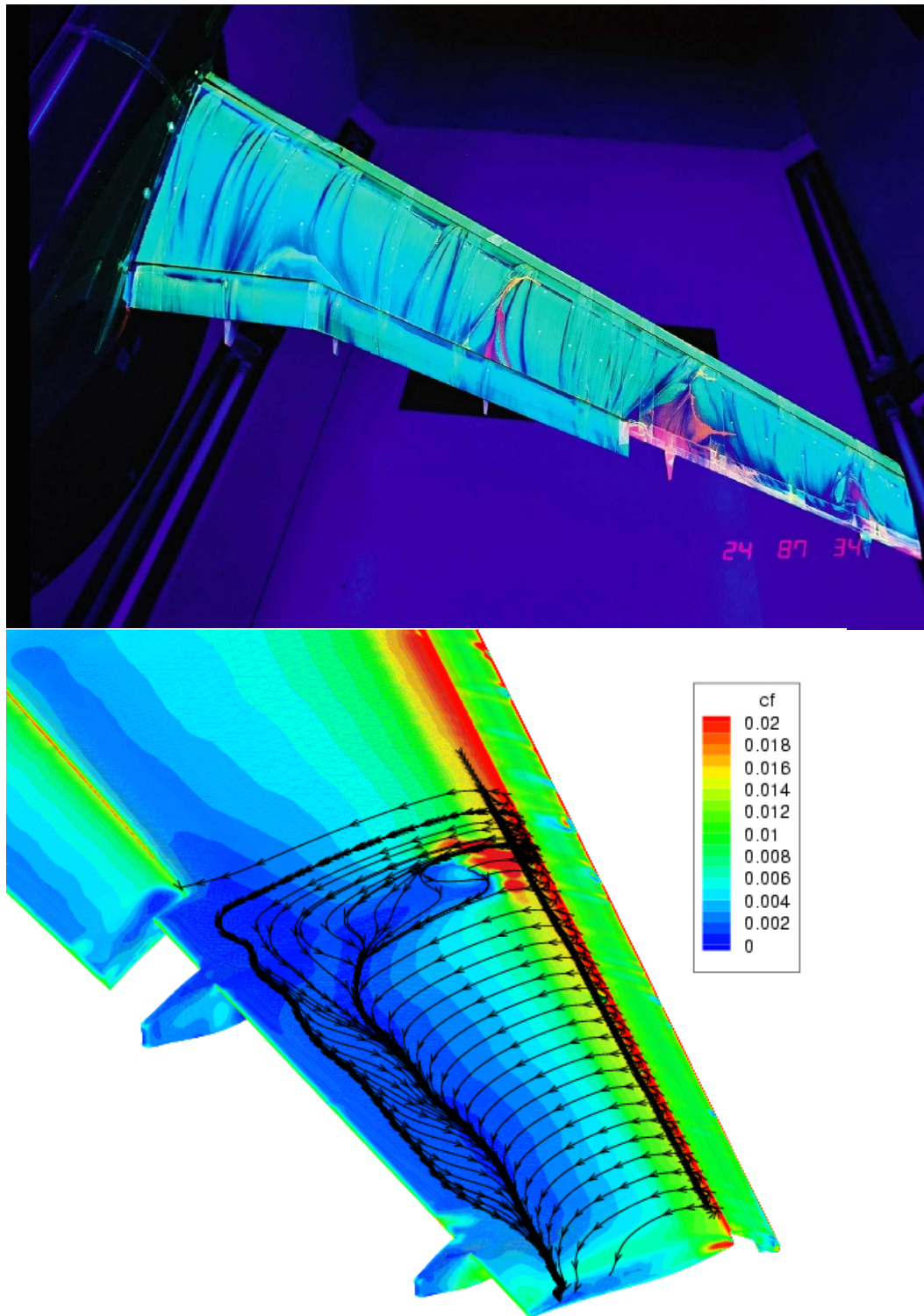


Figure 12 Comparison of the oil flow measurement of the KH3Y model for  $\alpha=18.5^\circ$  in LSWT (top) and the computed skin friction lines  $\alpha=16^\circ$  (on a refined computational hybrid grid); A flow separated area on the upper outboard wing at the position of the fourth flap track fairing is present both in experiment and in the computation.

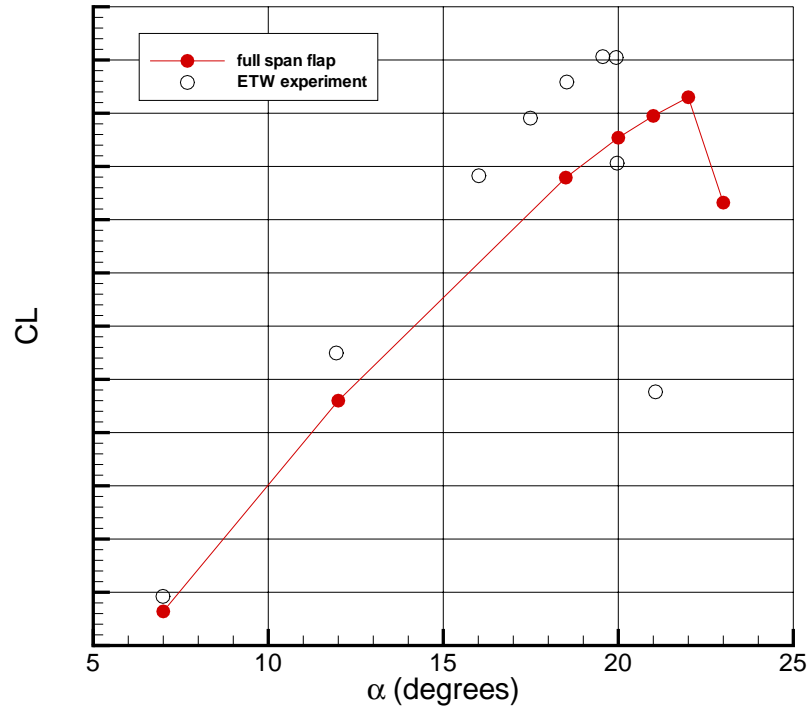


Figure 13 Comparison of the computed and measured lift curve (in ETW) for a full span flap high-lift configuration.

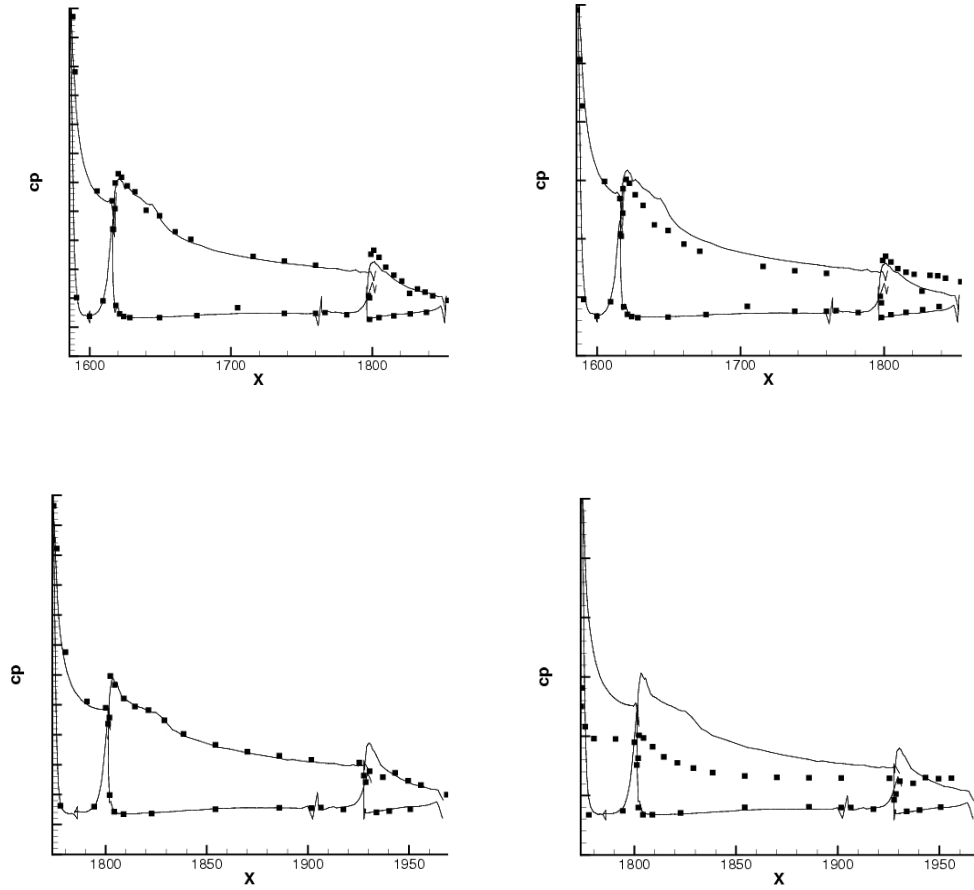


Figure 14 Comparison of the computed (line) and the experimental (points) pressure coefficient distributions for the full span flap configuration at high Reynolds number conditions (ETW) at section DV6 (upper) and DV10 (lower) for two angles of attack:  $\alpha=18.5^\circ$  (left),  $\alpha=20^\circ$  (right).

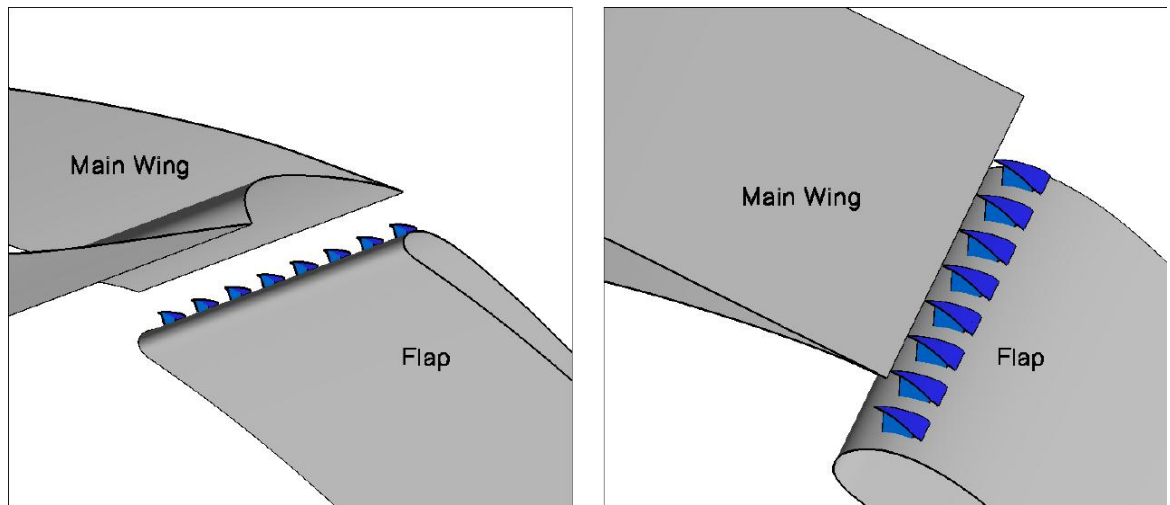


Figure 15 Sketch of the Free Flying Delta Array flow control device. The delta wings are mounted on top of the the leading edge of the flap.

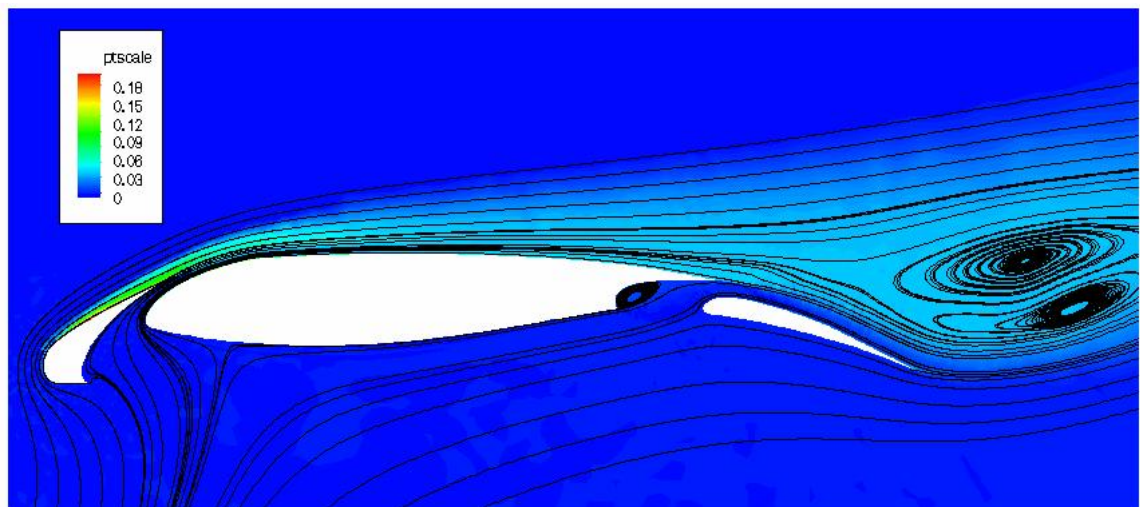


Figure 16 Illustration of wake break-up above the flap as computed for a HELIX baseline three element airfoil in take-off configuration at  $M_\infty = 0.20$ ,  $\alpha = 32^\circ$  and  $Re = 21.0 \times 10^6$ . The flow field has been computed using a three-dimensional unstructured grid approach with periodical boundary conditions employed in spanwise direction. Note that: no delta arrays have been mounted for this case.

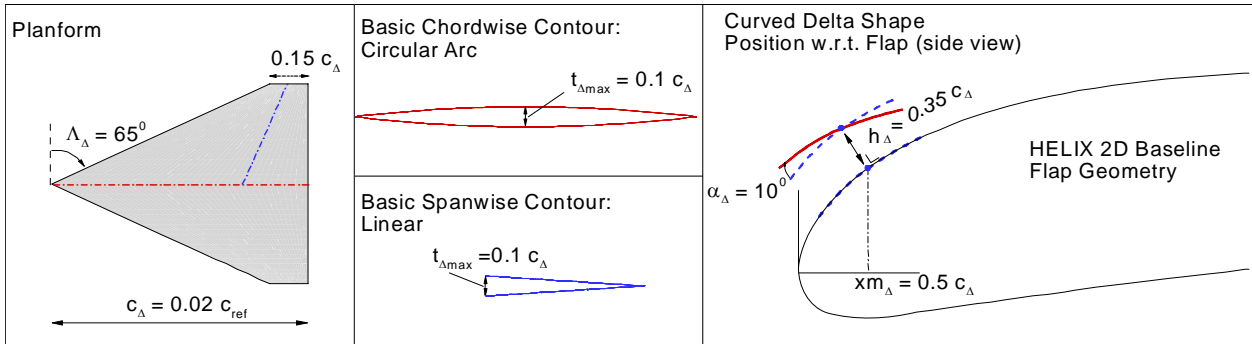


Figure 17 Geometric design of the FFDA delta wing shape

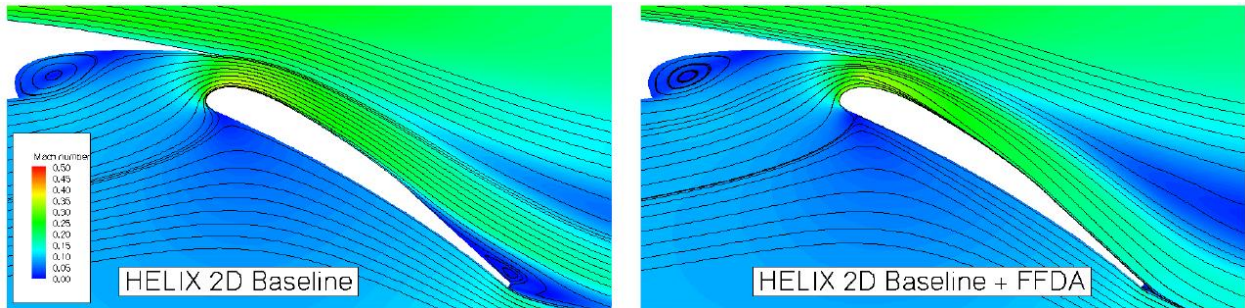


Figure 18 Comparison of stream patterns in the centre plane for the HELIX 2D baseline landing configuration with and without FFDA at  $M_\infty = 0.18$ ,  $\alpha = 18^\circ$  and  $Re = 19.0 \times 10^6$

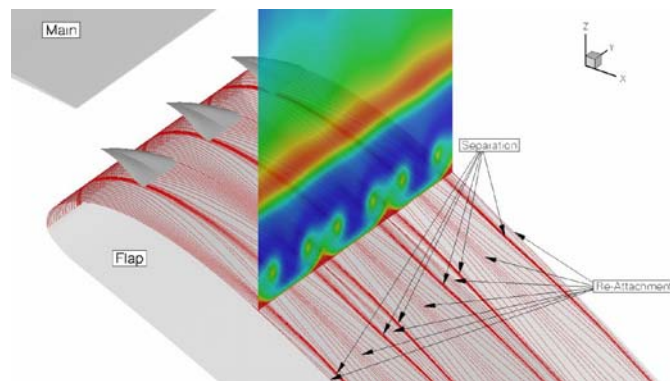


Figure 19 Flap limiting streamlines (integrated skin friction lines) and total-pressure-losses in a cross-flow plane for the HELIX 2D baseline landing configuration with Free Flying Delta Arrays installed at  $M_\infty = 0.18$ ,  $\alpha = 18^\circ$  and  $Re = 19.0 \times 10^6$ .

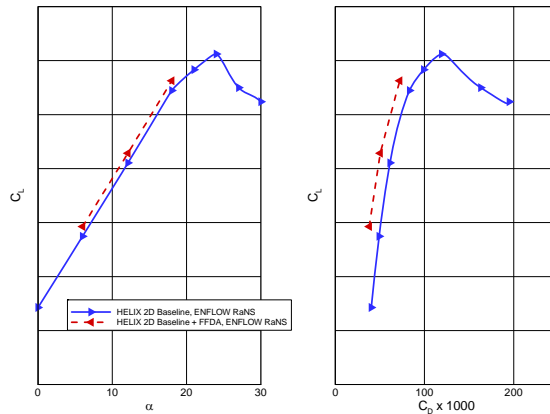


Figure 20 Lift vs. angle of attack and lift vs. drag for the HELIX 2D baseline landing configuration with and without FFDA at  $M_\infty = 0.18$  and  $Re = 19.0 \times 10^6$ .

Take-off Configuration ( $\delta_{slat} = 23^\circ$ ,  $\delta_{flap} = 22.3^\circ$ );  $M = 0.20$ ,  $Re = 4.66 \times 10^6 / m$

Landing Configuration ( $\delta_{slat} = 27^\circ$ ,  $\delta_{flap} = 35.0^\circ$ );  $M = 0.20$ ,  $Re = 4.66 \times 10^6 / m$

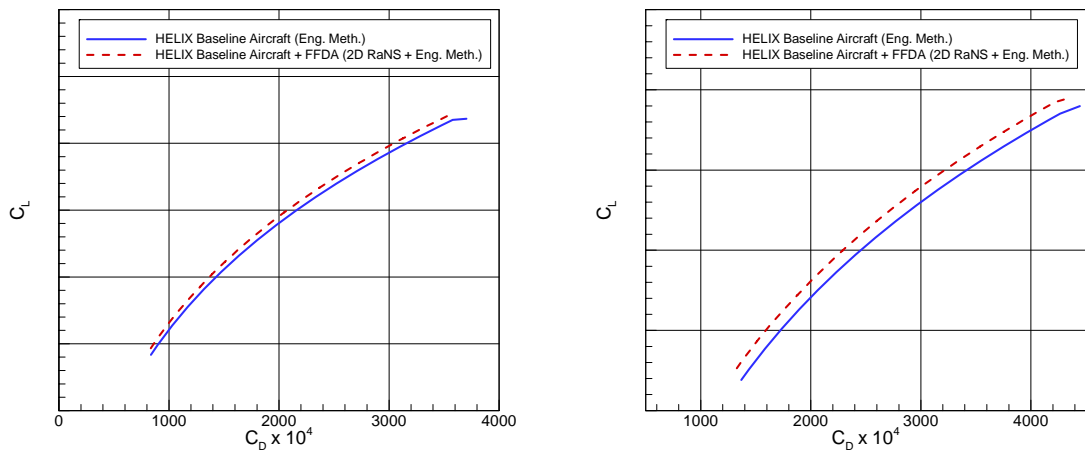


Figure 21 Estimated effect of the FFDA device on the drag polars of the HELIX baseline aircraft for take-off and landing configuration